Hysteresis Modeling of Magnetic Components With Generalized Distribution Function and Efficient Parameter Identification Based on Preisach Model

Zhan Shen, *Senior Member, IEEE*, Lexing Zhang, Shunshun Ma, Kaiyuan Liu, Xiao Yu, Jian Ai, Wei Qin, *Member, IEEE*, Fujin Deng, *Senior Member, IEEE*, Long Jin, and Wu Chen, *Senior Member, IEEE*

***Abstract*—Soft magnetic materials are widely used for magnetic components in power electronic converters. Their hysteresis effect leads to the nonlinear impedance characteristics of the magnetic cores, which can cause loss increase, waveform distortion, and electromagnetic interference issues in the converter. Due to the nonlinear behavior and the diversity of material characteristics, current Preisach hysteresis modeling remains challenging in parameter identification and probability distribution function (PDF) modeling procedure. In parameter identification, the classical methods rely on complex and restrictive double integration or repeated measurements. In PDF modeling, conventional PDF forms are constrained by a few degrees of freedom. To achieve high modeling precision, PDF forms with higher degrees of freedom are required. It also restricts the universality of the PDF, so different PDFs are needed for different magnetic materials. To address these two issues, a parameter identification approach based on the geometric interpretation of integration is proposed, which requires only a single *B–H* curve for ferrite. It avoids repeated testing and improves the identification efficiency significantly. Moreover, a generalized PDF form with more independent adjustable parameters is proposed. It can encompass different PDFs and model different hysteresis loop shapes of various magnetic materials. Experiments on different ferrites and silicon steels are conducted for verification. Compared with the conventional method, the proposed approach demonstrates significant improvements in accuracy, universality, simplification, and rapidity across different materials and shapes of magnetic cores.**

***Index Terms*—Hysteresis effects, parameter identification, Preisach model, probability distribution function (PDF), soft material.**

Received 7 August 2025; revised 31 October 2025; accepted 10 December 2025. Date of publication 15 December 2025; date of current version 20 March 2026. This work was supported in part by the National Key Research and Development Program of China under Grant 2022YFE0196300, in part by the National Natural Science Foundations of China under Grant 52207191, and in part by Science, Technology & Innovation Funding Authority (STDF) under Grant 46505. Recommended for publication by Associate Editor L. Gu. *(Corresponding author: Jian Ai.)*

Zhan Shen, Lexing Zhang, Shunshun Ma, Kaiyuan Liu, Wei Qin, Fujin Deng, Long Jin, and Wu Chen are with the School of Electrical Engineering, Southeast University, Nanjing 210096, China (e-mail: zhs@seu.edu.cn; lxzhang@seu.edu.cn; mss@seu.edu.cn; kyliu@seu.edu.cn; wqin@seu.edu.cn; fdeng@seu.edu.cn; jinlong@seu.edu.cn; chenwu@seu.edu.cn).

Xiao Yu is with the Institute of Electronic Engineering, China Academy of Engineering Physics, Mianyang 621999, China (e-mail: yuxiao@cqu.edu.cn).

Jian Ai is with the School of Internet of Things Engineering, Jiangnan University, Wuxi 214122, China (e-mail: jianai0204@jiangnan.edu.cn).

Color versions of one or more figures in this article are available at https://doi.org/10.1109/TPEL.2025.3644017.

Digital Object Identifier 10.1109/TPEL.2025.3644017

I. INTRODUCTION

SOFT magnetic materials are widely used in inductors and transformers for power converters [1]. These materials exhibit significant power losses, which affect overall system performance [2], [3]. Moreover, practical power electronics requirements such as low cost, compact size, and high power density drive magnetic components to operate near saturation regions [4], [5], [6], [7]. In such nonlinear regions, neglecting hysteresis and saturation effects can lead to significant errors in modeling and control of converters. In [8], by considering magnetic saturation in the inductor of a buck converter, the calculation error of the inductor current decreases significantly from 60.2% to 1.88%, and the error of the estimated capacitor value is reduced from 79.5% to as low as 4.37%. Therefore, accurate modeling of soft magnetic materials is essential for both the design optimization and transient equivalent circuit modeling of power electronic converters.

Currently, modeling methods for soft magnetic materials can generally be categorized into four types: Steinmetz equation-based models, loss separation models, neural network-based models, and hysteresis models [9], [10], as is summarized in Table I. Steinmetz equation-based methods, due to its few parameters and simple structure, are convenient for industrial application [11], [12]. However, such empirical formulations fail to capture the underlying loss mechanisms and their spatial distribution within the magnetic core, and they tend to produce significant errors under nonsinusoidal excitation conditions [9]. Bertotti divided the total core loss into hysteresis loss, eddy current loss, and excess loss [13]. Nevertheless, in practical applications, excess loss is often treated merely as the discrepancy between measured and calculated values, making its physical origin ambiguous and thus depriving the model of clear physical interpretability. In recent years, data-driven neural network models have gained popularity owing to their high prediction accuracy [14], [15]. However, these approaches transform the computation of core losses into a black-box process, lacking physical interpretability and heavily dependent on large training datasets. Hysteresis models are derived from the intrinsic properties of magnetic materials and their magnetization processes, including the Jiles–Atherton (JA) model, Stoner–Wohlfarth (SW) model, and Preisach model [16], [17], [18]. These models possess concise mathematical forms and clear physical

TABLE I
CHARACTERISTICS OF DIFFERENT MAGNETIC MODELING MODELS

Magnetic modeling model	Physical interpretability	Complexity	Accuracy of core loss modeling	Applicable to transient circuit analysis
Steinmetz equation-based method	Weak [19], [20]	Simple [9], [10]	High in narrow range [9]	Low
Loss separation model	Weak [19], [20]	Simple [9], [10]	High [9]	Low
Neural network-based model	Weak [19], [20]	Very complex [10]	Very high [10], [14]	Limited to PWM transient excitation [21]
Hysteresis model	Strong [19], [20]	Moderate [9], [10]	High [9]	High (Preisach model) [22], [23]

TABLE II
CHARACTERISTICS OF DIFFERENT HYSTERESIS MODELS

Hysteresis model	Computational complexity [25], [26]	Ability to capture minor loops and path dependence [25], [26]	Parameter identification complexity [25], [26]	Applicable to transient circuit analysis [25], [26]
Jiles-Atherton model [16]	Moderate	Limited	Moderate	Moderate
Stoner-Wohlfarth model [17]	Simple	Limited	Simple	Limited
Preisach model [18]	High	Strong	Difficult	High [22], [23]

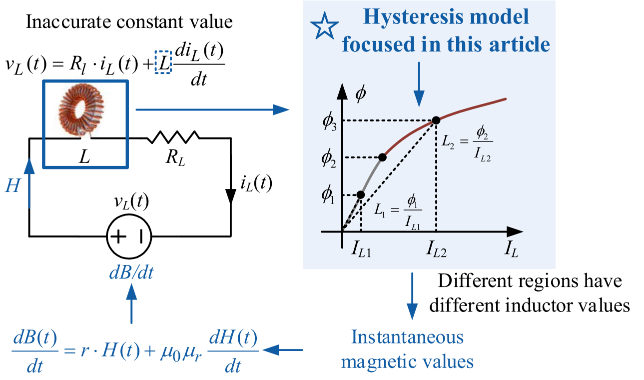

Fig. 1. Transient simulation analysis of the analytical model in magnet challenge 2 [24].

meanings, yet their parameters are often difficult to identify accurately.

Table I presents a comparison of the characteristics of existing magnetic modeling approaches. The first three methods can only provide scalar loss results with sinusoidal or limited waveforms. Under transient excitation of different waveforms, they fail to model nonlinear *B-H* behavior, and cannot be integrated into circuit-level equivalent circuit modeling of power electronic converters. As shown in Fig. 1, the analytical model in Magnet Challenge 2 essentially converts electrical components into their magnetic counterparts [24]. In contrast, hysteresis models, which are based on the intrinsic properties of magnetic materials and magnetic excitation, provide expressions of magnetic characteristics such as instantaneous permeability that perfectly correspond to the magnetic quantities required by the analytical model. Therefore, they are widely used for core loss prediction, nonlinear *B-H* curve modeling, and transient circuit analysis for power electronic converters [22], [23].

Among the hysteresis modeling approaches, the Preisach model has been widely applied due to its superior accuracy and ability to capture path dependence compared with the other JA model and SW model, as shown in Table II. Specifically, the JA model explains hysteresis phenomena based on the movement of domain walls. For highly nonlinear operation regions and high-frequency applications, the JA model struggles to describe complex hysteresis behavior. The SW model is simple and easy to use, but it cannot reflect the historical effects of magnetization or path dependence. In contrast, the Preisach model offers higher accuracy, which can describe complex hysteresis loops and their path dependence precisely. Hence, the Preisach model is widely used in hysteresis modeling [25], [26], and is the focus of our study.

In recent years, numerous studies have been devoted to improving the Preisach model. Current research on the Preisach model mainly focuses on its application in circuit-level system simulations under different scenarios. In [23], Luo et al. implement the Preisach model in circuit-level system simulations through a permeance–capacitance analogy. In [22] and [27], Luo et al. further introduce frequency-dependent loss characteristics. In [28], Djekanovic et al. explore a time-domain Preisach model considering temperature variations. Nevertheless, for frequency-independent hysteresis modeling, the accuracy and efficiency of the Preisach model are still largely constrained by two key challenges, i.e., its parameter identification procedure and the probability distribution function (PDF) [29]. However, none of the above studies have specifically addressed these two issues, which will be analyzed in detail below.

Parameter identification is the key procedure in Preisach modeling, which requires both accuracy and computational efficiency. The conventional continuous Preisach model employs time-consuming double integration of the PDF in parameter identification. It focuses on the characteristic points of the *B-H* curve, which leads to poor modeling accuracy [30]. Moreover, double integration requires integrating the PDF analytically, which restricts the form of the PDF. Therefore, the discrete Preisach model is employed to convert the double integration into discrete numerical addition and subtraction operations. It focuses on the overall *B-H* curve rather than several characteristic points, thereby significantly improving the accuracy in parameter identification. Various approaches have been developed for the discrete Preisach model. In [31], a genetic algorithm-based parameter identification method is proposed, but it needs 15 minute convergence time and is inefficient. In [32], an analytical discretization-based parameter identification method using the Everett function is proposed. However, it has a poor fit of inner loops. In [33] and [34], the (U, V) plane is uniformly discretized, requiring a large number of measured hysteresis loops with different field amplitudes to achieve acceptable resolution. Although this method can capture the hysteresis behavior of a wide range of magnetic materials, it requires many repeated measurements to maintain an accuracy level. Moreover, the numerically constructed PDF lacks physical meaning. In conclusion, a general, efficient, and precise parameter identification method is still missing for the Preisach model.

The PDF is essential to model the shape of *B-H* curves, and many efforts have been made to explore suitable PDF forms of different materials to improve modeling accuracy. Azzerboni et al. [35] use the Lorentz PDF with three degrees of freedom as the distribution function for nonoriented steels. However, for ferrite materials, Lorentz PDF results in significant errors on the equivalent magnetic permeability and per-cycle energy loss. In [36], Szabó and Füzi proposed the Cosh PDF with three degrees of freedom for ferromagnetic cores, using the extreme values of concentric hysteresis loops to express the magnetic flux density in a closed form. However, the Cosh PDF leads to poor fitting of the inner loops. To compensate for the accuracy loss, additional complex computations are required. Luo et al. [23] use the logistic PDF, which also has three degrees of freedom, but it is limited to ferrite materials. To conclude, current PDFs are only for specific materials, with limited three degrees of freedom, and cannot balance between the accuracy and computational burdens. A generic PDF is needed to capture the materials' nonlinearity and enhance the flexibility in handling different complex hysteresis loops.

To overcome the aforementioned two challenges, this article proposes a novel parameter identification method based on the discrete Preisach model and the geometric interpretation of integration. It simplifies the computation process and provides a general approach applicable to any PDF, which avoids restrictive double integration and repeated *B-H* curve measurements in the classical approach. Moreover, a generalized distribution function is proposed for complex hysteresis modeling. It is applicable to various soft magnetic materials, thanks to the novel implementation method that enhances the adaptability and accuracy of the Preisach model.

The rest of this article is organized as follows. Section II reviews the classical Preisach model, its discretization approach, and the related issues. In Section III, an efficient and generic parameter identification method is proposed based on the Levenberg–Marquardt (LM) algorithm. The proposed PDF and its sensitivity analysis are in Section IV. Section V evaluates the proposed implementation method on various soft magnetic materials and compares the results with two conventional Preisach models. The proposed method's simplification and accuracy, as well as its extensibility and potential future research directions, are discussed in Section VI. Finally, Section VII concludes this article.

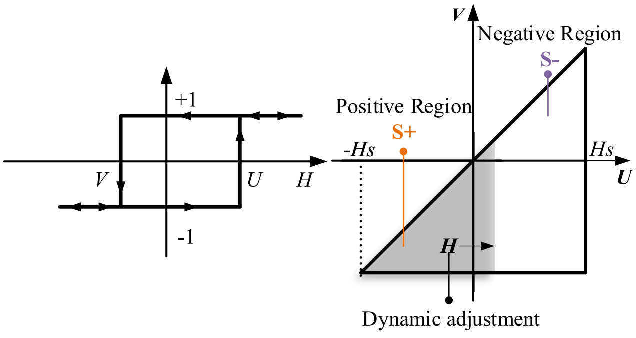

(a) (b)

Fig. 2. (a) Single hysteresis operators $\gamma(U, V)$ of the Preisach Model. (b) Variable integration region of the classical Preisach model.

II. CLASSICAL PREISACH MODEL AND ITS ISSUES

A. *Brief Review of Classical Preisach Model*

The classical Preisach model assumes that soft magnetic materials consist of numerous dipoles, which are abstracted as hysteresis operators $\gamma(U, V)$ [25]. In Fig. 2(a), U and V are the upper and lower switching threshold values, respectively, which determine the transition of each square-loop $\gamma(U, V)$ between -1 and $+1$. The switching positions of these hysteresis operators follow a specific distribution law as the PDF. The flux density B is expressed as the weighted summation of all hysteresis using a PDF, and the two-dimensional PDF $p(U, V)$ can be expressed as the product of two one-dimensional PDFs, i.e., $p_s(U)$ and $p_s(-V)$

$$\begin{aligned} B &= \iint p(U,V)\cdot\gamma(U,V)dUdV \\ &= \iint p_s(U)\cdot p_s(-V)\cdot\gamma(U,V)dUdV. \end{aligned} \tag{1}$$

In Fig. 2(b), the integral region is a triangular area with $U = V$ as its boundary, the integral region dynamically adjusts the positive and negative integration areas based on the input signal as the dividing line. $S+$ and $S-$ denote the integrals over positive and negative regions. In "$S+$" region, $\gamma = +1$, while in "$S-$" region, $\gamma = -1$. The flux density B is calculated as

$$\begin{aligned} B = 2&\iint_{S+} p_s(U)\cdot p_s(-V)dUdV \\ &- \iint_{S} p_s(U)\cdot p_s(-V)dUdV \end{aligned} \tag{2}$$

where S is the integral over the entire region.

B. *Conventional Parameter Identification Issues*

In parameter identification, the classical continuous and discrete form modeling are challenging in terms of accuracy and

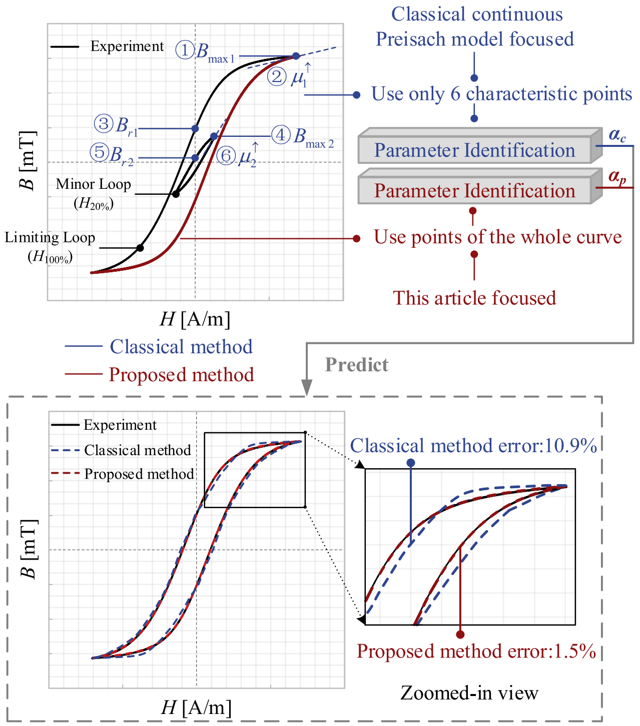

Fig. 3. Classical continuous Preisach model issues. The blue components represent the classical method, while the red components correspond to the proposed one. Under the same choice of PDF, α_c and α_p represent the parameters obtained from two different parameter identification processes, resulting in a significant performance difference.

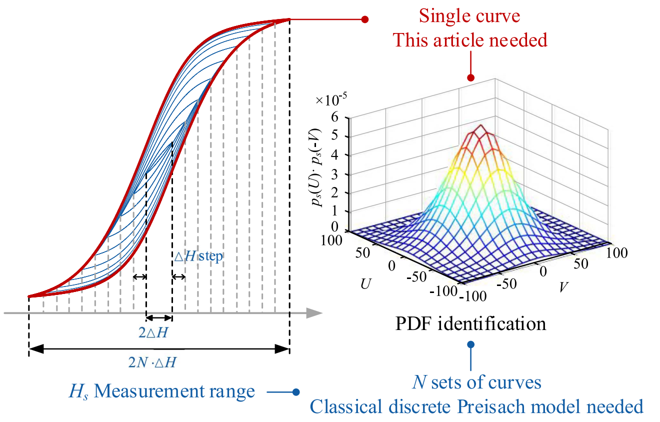

Fig. 4. Classical discrete Preisach model issues. The classical method requires repeated measurements for N sets of experiments, whereas the proposed method requires only one measurement of the limiting hysteresis loop.

computational complexity, respectively. First, in the continuous Preisach model, the conventional double integral method is typically solved analytically and can only handle simple PDFs. When the function becomes more complex, it cannot be solved analytically. Moreover, as shown in Fig. 3, we define the one with the largest field strength amplitude H_s (e.g., 100 A/m), which makes the flux density approach saturation, as the "limiting loop." The conventional continuous Preisach model performs parameter identification based on a limited set of characteristic points from the limiting and minor hysteresis loops, such as the peak magnetic field strength ($B_{\max}$), remanent flux density (B_r), and permeability on the ascending branch ($\mu^{\uparrow}$). The classical approach may easily become trapped in a local optimum, resulting in poor accuracy across the rest of the hysteresis loop. In contrast, the implementation proposed in this article considers every sampled experimental data point along the ascending branch, enabling global optimization of the complete hysteresis behavior. The detailed procedure will be presented in Section III. In [23], a logistic PDF-based Preisach model is used to describe the hysteresis behavior of 3F3 ferrite under a magnetic field strength of 100 A/m, yielding a per-cycle energy loss error of 10.9%. The original approach exhibits significant deviation when capturing the large curvature of the 3F3 hysteresis loop. In comparison, when the proposed parameter identification method is adopted, the corresponding error reduces to 1.5%, as illustrated in the lower part of Fig. 3.

Second, the classical discrete Preisach model is of high complexity. On the right side of Stage II in Fig. 5, a bounded triangular Preisach model is illustrated, where the Preisach plane is discretized with a level $N = 10$. Within the Preisach plane, the PDF $p(U, V)$ for each square region is concentrated at the lower-left corner of the square. For the classical Preisach model, a discrete expression is required [37], [38]

$$B = \sum_{i=1}^{N_t} W_i H_i \tag{3}$$

where W_i denotes the weight, H_i is the output of a relay operator, and N_t is the total number of hysteresis operators. During the numerical discretization of the Preisach model, the weight W_i is assigned based on the number of discrete grid divisions, which requires N sets of B–H curve measurements to construct the discretized PDF. To achieve acceptable accuracy, the discretization level of $N = 10$ used in this example is far from sufficient, and a significantly larger number of repeated measurements would be required. This is impractical from an engineering perspective, as illustrated in Fig. 4.

To conclude, neither the discrete nor the continuous Preisach mode can achieve a balance between model accuracy and computational complexity. Therefore, a more generalized, accurate, and effective parameter identification method is required, as introduced in Section III.

C. Conventional PDF Issues

The hysteresis loops of soft magnetic materials typically exhibit "S" shaped curves. Based on this characteristic, the Logistic and Lorentz functions are proposed as the PDFs in (1)

$$p_s^{\text{Logistic}}(x) = A \cdot \frac{e^{-(x-H_0)\sigma}}{\left(1+e^{-(x-H_0)\sigma}\right)^2} \tag{4}$$

$$p_s^{\text{Lorentz}}(x) = A \cdot \frac{1}{1+(x-H_0)^2\sigma}. \tag{5}$$

However, these PDFs only have three degrees of freedom: A (scaling), H_0 (location), and σ (shape), which limit their fitting accuracy. The Lorentz PDF features a long tail but lacks flexibility to adjust skewness or kurtosis, resulting in a rigid

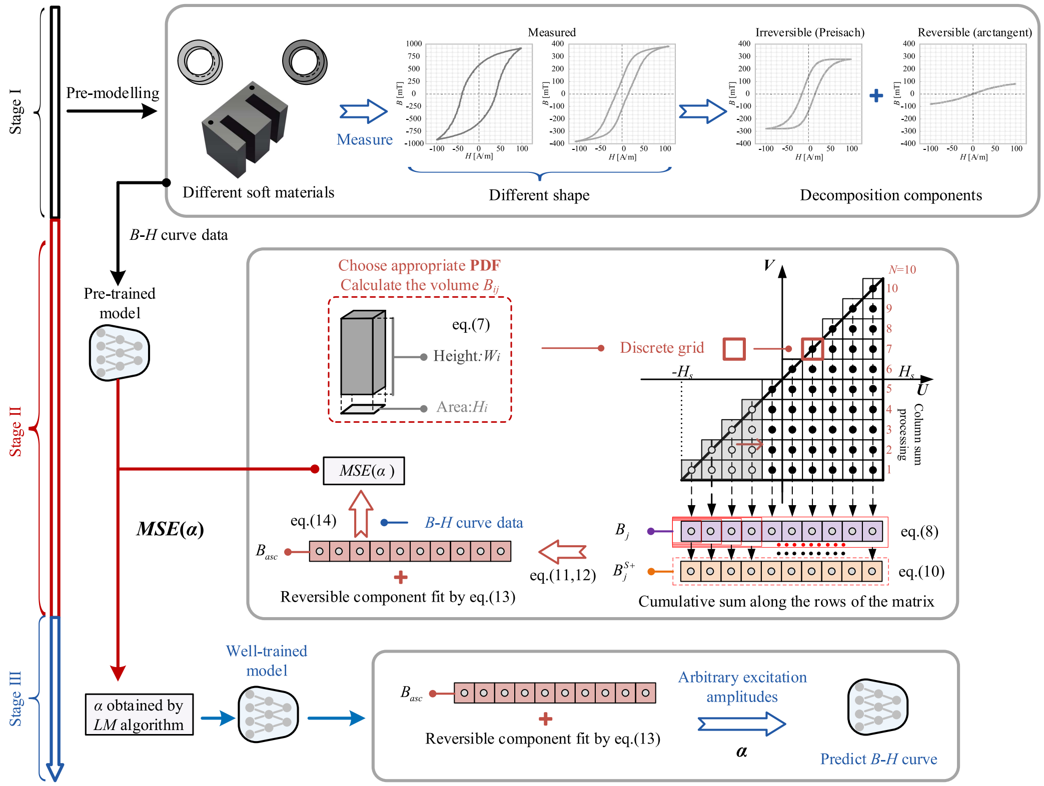

Fig. 5. Parameter identification and hysteresis modeling based on the discrete Preisach model.

shape. The Logistic PDF is symmetric and unimodal, but it struggles to capture complex distribution characteristics such as sharp peaks, heavy tails, and local asymmetries. With the increasingly complex hysteresis of emerging magnetic materials, these low-degree-of-freedom PDFs have gradually revealed their inherent limitations.

Furthermore, different soft magnetic materials require different PDFs for their respective hysteresis loops, which significantly reduces the adaptability of the model. Hence, a generalized PDF with a high-degree-of-freedom and enhanced representational capacity is proposed in Section IV.

III. GENERAL METHOD FOR PARAMETER IDENTIFICATION OF DISTRIBUTION FUNCTIONS

In this section, a parameter identification method applicable to arbitrary PDFs is proposed, which requires only a single set of experimental data for ferrite. This method integrates numerical integration with the LM fitting algorithm. It is an optimization procedure aimed at fitting the *B-H* curve as closely as possible to the given data. This is achieved by globally optimizing the parameters of the PDF to minimize the curve fitting error, without the need to solve the double integral analytically.

The parameter identification and hysteresis modeling procedure include three parts, i.e., acquiring *B-H* curve data, grid partitioning for obtaining the objective function, and parameter identification via LM algorithm, which is introduced in detail below.

A. Stage I: Acquiring B-H Curve Data Including Reversible and Irreversible Components

As shown in Fig. 5, the *B-H* curves of different soft magnetic materials are measured before model training. The detailed measurement procedure is described in Section V. In [39], the *B-H* curve can be decomposed into reversible and irreversible components. The irreversible component is characterized by the Preisach model, while the reversible component essentially represents a single-lined *B-H* characteristic, which can be expressed using an arctangent function. The measured data are then input into the pretrained model for further analysis.

B. Stage II: Grid Partitioning for Obtaining the Objective Function

In Stage II, the variable integration ranges from $-H_s$ to H_s is divided into N equal parts, resulting in a discretized lower triangular region in Fig. 5. Subsequently, an $N \times N$ lower triangular unit matrix A_N^N is constructed as follows:

$$A_N^N = \begin{bmatrix} 0 & \cdots & 0 & 0 & 1 \\ 0 & \cdots & 0 & 1 & 1 \\ 0 & \cdots & 1 & 1 & 1 \\ \vdots & \ddots & \vdots & \vdots & 1 \\ 1 & \cdots & 1 & 1 & 1 \end{bmatrix}. \tag{6}$$

We define the step size after dividing the interval, i.e., step $= \frac{2H_s}{N}$. After discretizing the variable integration region, the integral can be transformed into the summation and subtraction of integrals over each discrete grid cell. Each grid integral can be regarded as the volume of a rectangular prism, where H_i in (3) corresponds to the base area, a square region with an area of step^2, and W_i in (3) represents the height, defined as the product of two one-dimensional PDFs. This equivalence originates from (1) and carries clear physical significance.

Express this equivalence in matrix form, define U as the row vector obtained by dividing the interval $[-H_s, H_s]$, and V can be defined as the transpose of U. Thus, the volume of each square grid region can be calculated as

$$B_{ij} = \left[p_s(U) \cdot p_s(-V) \cdot \text{step}^2\right] \cdot A_N^N \tag{7}$$

where B_{ij} represents the integration region of the Preisach model as a lower triangular matrix. The PDF is concentrated at the lower-left corner of the discrete grid squares.

In the Preisach model, the hysteresis loop is symmetric, so it is sufficient to fit either the ascending or descending branch. In Fig. 5, the ascending branch is taken as an example. The grey region represents the positive integral, and the white region represents the negative integral. This is one possible scenario during the variation of H.

Then, by summing the values of grid by column, the accumulated value B_j is obtained as follows:

$$B_j = B_{ij}^T C \tag{8}$$

$$C^T = [\begin{matrix} 1 & 1 & \cdots & 1 \end{matrix}]. \tag{9}$$

In different cases, the first term in (2) is represented as B_j^{S+}

$$B_j^{S+} = \sum_{k=1}^{j} b_j^k \tag{10}$$

where H_j is the magnetic field strength of the jth data point among N input data. b_j^k is the kth row element of B_j.

The second term in (2) is the sum of all the elements in the lower triangular matrix, which can be represented as B_j^S

$$B_j^S = C^T B_{ij} C. \tag{11}$$

Therefore, in the discrete Preisach model, for the ascending curve, (2) can be represented as $B_{\text{asc}}(H_j)$

$$B_{\text{asc}}\left(H_j\right) = 2B_j^{S+} - B_j^S. \tag{12}$$

There is also reversible magnetization in soft magnetic materials, which cannot be captured by the irreversible Preisach model. Therefore, the modeling should also consist of a reversible component modeled by the arctangent function

$$B_{\text{rev}}\left(H_j\right) = K_1 \cdot \arctan\left(K_2 \cdot H_j\right) \tag{13}$$

where K_1 and K_2 are parameters to be determined. Taking the experimental data $B_{\exp}$ as the target dataset, and denoting α as the unknown parameters in the PDF and reversible component parameters, the mean squared error (MSE) used as the loss function can be expressed as

$$\text{MSE}(\alpha) = \frac{1}{N}\sum_{j=1}^{N}\left[B_{\exp}(j) - B_{\text{asc}}\left(H_j\right) - B_{\text{rev}}(H_j)\right]^2$$

$$= \frac{1}{N}\sum_{j=1}^{N}\left[B_{\exp}(j) - B_{\text{asc}f}\left(H_j, \alpha\right)\right]^2 \tag{14}$$

where $B_{\exp}(j)$ is the jth measured value of the magnetic flux density, $B_{\text{asc}f}$ is the final ascending curve with the reversible component.

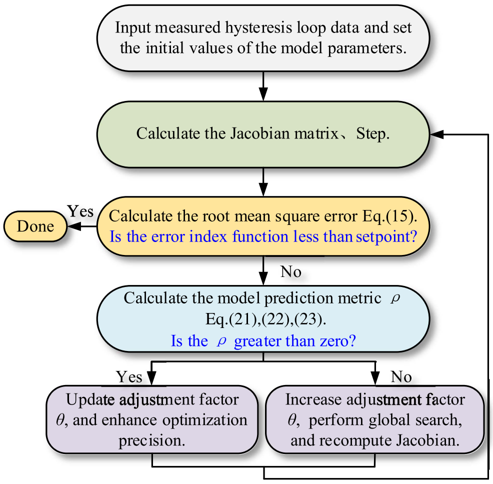

Fig. 6. Flowchart of parameter identification using the LM algorithm.

C. Stage III: Proposed Parameter Identification Via LM Algorithm

Fig. 6 illustrates the proposed parameter identification flowchart based on the LM algorithm, which is an improved *Gauss-Newton* method to solve nonlinear matrices. Compared with other fitting algorithms, this algorithm achieves a balance between the fast convergence of the gradient descent method and the robustness of the Newton method, allowing it to converge even with poor initial values [40]. The optimal parameter vector is obtained by solving the minimization problem of the loss function MSE(α), aiming to achieve the best possible fit to the experimental data. The objective function of LM can be expressed as follows:

$$\min_{\alpha} S\left(\alpha\right) = \min_{\alpha} \text{MSE}(\alpha)$$

$$= \min_{\alpha} \frac{1}{N}\sum_{j=1}^{N}\left[B_{\exp}(j) - B_{\text{asc}f}(H_j, \alpha)\right]^2 \tag{15}$$

where parameter vector $\alpha = [\alpha_1, \alpha_2, \ldots, \alpha_M]^T$, $(H, B_{\exp})$ is a vector set of data pairs that contains N elements, and $B_{\text{asc}f}$ is a series of approximation functions. The objective function can be rewritten as follows:

$$\hat{\alpha} = \arg\min_{\alpha} S(\alpha) = \arg\min_{\alpha} \|r(\alpha)\|_2^2 \tag{16}$$

$$r(\alpha) = [r_1(\alpha), r_2(\alpha), \ldots, r_N(\alpha)]^T \tag{17}$$

where $r(\alpha)$ is residual vector. The *Gauss-Newton* iterative equation is expressed as follows:

$$\begin{cases} \alpha_{k+1} = \alpha_k + \Delta\alpha_k \\ \triangle\ \alpha_k = -\left[J(k)^T J(k)\right]^{-1} J(k)^T r(\alpha_k) \\ \Delta\alpha_k = \left[\alpha_{k+1,1} - \alpha_{k,1}, \ldots, \alpha_{k+1,M} - \alpha_{k,M}\right]^T \end{cases} \tag{18}$$

where α_k and α_{k+1} are the input vectors at the kth and $(k+1)$th iterations, respectively, and $\Delta\alpha_k$ denotes the change from the kth iteration to the $(k+1)$th iteration. $\alpha_{k,p}$ is the pth parameter of vector $\alpha_k (1 \le p \le M)$.

However, the *Gauss–Newton* method suffers from poor robustness and is sensitive to the choice of the initial point, which may lead to convergence failure in certain cases. To improve the performance of the algorithm, adjustment factor θ is introduced. The LM iterative equation can be expressed as follows:

$$\begin{cases} \alpha_{k+1} = \alpha_k + \Delta\alpha_k \\ \Delta\alpha_k = -\left[J(k)^T J(k) + \theta^{(k)} I\right]^{-1} J(k)^T r(\alpha_k) \end{cases} \tag{19}$$

where I is the unit matrix. $J(k)$ is the Jacobian matrix of $r(\alpha_k)$ and is calculated as follows:

$$J(k) = \frac{\partial r(\alpha_k)}{\partial \alpha_k} = \begin{bmatrix} \frac{\partial r_1(\alpha_k)}{\partial \alpha_{k,1}} & \frac{\partial r_1(\alpha_k)}{\partial \alpha_{k,2}} & \cdots & \frac{\partial r_1(\alpha_k)}{\partial \alpha_{k,M}} \\ \frac{\partial r_2(\alpha_k)}{\partial \alpha_{k,1}} & \frac{\partial r_2(\alpha_k)}{\partial \alpha_{k,2}} & \cdots & \frac{\partial r_2(\alpha_k)}{\partial \alpha_{k,M}} \\ \vdots & \vdots & \ddots & \vdots \\ \frac{\partial r_N(\alpha_k)}{\partial \alpha_{k,1}} & \frac{\partial r_N(\alpha_k)}{\partial \alpha_{k,2}} & \cdots & \frac{\partial r_N(\alpha_k)}{\partial \alpha_{k,M}} \end{bmatrix}. \tag{20}$$

In LM algorithm, θ is adjusted adaptively to ensure the parameters can be converged to exact solutions quickly. To avoid error-prone caused by an arbitrary selection, the adjustment factor θ is updated by ρ, which can be expressed as follows [41]:

$$\begin{cases} \theta^{(k)} = \theta^{(k-1)} \times \max\left\{\frac{1}{3}, 1 - (2\rho - 1)^3\right\}, \rho > 0 \\ \theta^{(k)} = \theta^{(k-1)} \times 2, \rho \le 0 \end{cases} \tag{21}$$

$$\rho = \frac{S(\alpha_k) - S(\alpha_{k-1})}{L_{k-1}(\triangle\ \alpha_{k-1}) - L_{k-1}(0)} \tag{22}$$

$$L_{k-1}(\triangle\ \alpha_{k-1}) = S(\alpha_{k-1}) + 2r(\alpha_{k-1})^T J(k-1) \triangle\ \alpha_{k-1} + (\triangle\ \alpha_{k-1})^T J(k-1)^T J(k-1) \triangle\ \alpha_{k-1}. \tag{23}$$

For each updated parameter vector α_k, ρ is computed according to (22), (23), and the adjustment factor θ is subsequently modified based on (21). The parameter ρ, defined as the ratio of actual improvement to predicted improvement, serves as a metric for evaluating the degree of model refinement. If ρ is greater than zero, it indicates that the iteration has yielded improvement, and a smooth adaptive strategy is employed to appropriately adjust θ to enhance optimization precision. Conversely, if ρ is less than or equal to zero, suggesting a degradation in iterative performance, θ is increased to facilitate broader exploration of the parameter space. The optimization process continues until the objective function falls below a predefined error threshold.

After the iterative process converges, the globally optimized parameter vector α is used as inputs, and the Preisach model becomes well-trained, as illustrated in Stage III of Fig. 5. At this point, all the unknown parameters in (12) and (13) have been determined, enabling accurate prediction of the *B-H* curve at arbitrary excitation amplitudes.

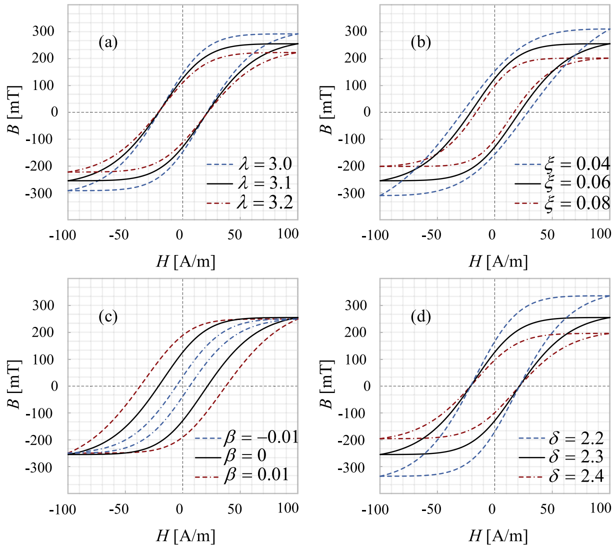

Fig. 7. Impact of function parameters on the hysteresis loops. By adjusting the four degrees of freedom, the hysteresis model of the core can be modeled.

IV. A GENERIC PDF FOR DIFFERENT MAGNETIC MATERIALS

To further improve the accuracy and efficiency in applying different PDFs for different magnetic materials, it is necessary to construct a generalized distribution function used in Stage II. This section introduces a generalized PDF capable of encompassing the majority of existing PDFs. Moreover, the influence of its parameters on the shape and characteristics of the hysteresis loop is analyzed in detail.

A. Proposed Preisach Distribution Function

The generalized hyperparameter (GH) PDF is a highly extensible distribution model used in the fields of statistics and machine learning. It is adopted in this work to model hysteresis for different materials. Compared to conventional PDFs, the GH PDF significantly enhances the capability of modeling complex data patterns by incorporating a higher number of degrees of freedom. The core concept of the function is to increase the number of parameters or to introduce additional control variables to achieve superior fitting performance in complex real-world applications. Hence, the function *f(x)* is used as the new PDF in (1)

$$f(x) = \frac{(\xi^2 - \beta^2)^{\lambda/2}}{\sqrt{2\pi}\xi^{\lambda-0.5}\delta^{\lambda} K_\lambda\left(\delta\sqrt{\xi^2 - \beta^2}\right)} \times e^{\beta(x-u)} \times \left[\frac{\sqrt{\delta^2 + (x-u)^2}}{\delta}\right]^{\lambda} \times K_\lambda\left[\xi\sqrt{\delta^2 + (x-u)^2}\right]. \tag{24}$$

Below are the parameter descriptions, as illustrated in Fig. 7.

TABLE III
EFFECT OF PARAMETERS ON CHARACTERISTICS OF HYSTERESIS CURVE

Parameters	B_r	H_c	B_{max}
$\lambda\uparrow$	↓	—	↓
$\zeta\uparrow$	↓	↓	↓
$\beta\uparrow$	↑	↑	—
$\delta\uparrow$	↓	—	↓

1) λ, shape parameter: It determines the overall shape of the distribution, especially the behavior of the tails. A larger value of λ typically results in a distribution that closely approximates the normal distribution, whereas smaller or negative values of λ tend to produce heavier tails, thereby increasing the likelihood of extreme values.
2) ζ, scale parameter: It controls the scale of the distribution, affecting the peak sharpness and thickness of the tails. A larger ζ leads to a more pronounced peak and thinner tails, making it resemble the shape of a normal distribution. In contrast, a smaller ζ increases the thickness of the distribution tails.
3) β, skewness parameter: It controls the asymmetry of the distribution, that is, the degree of skewness. A positive value of β results in a right-skewed distribution, while a negative β causes left skewness. Skewness implies that the distribution has a longer tail on one side.
4) δ, extent parameter: It controls the extent of the distribution. As δ increases, the distribution becomes more spread out and flatter, whereas a smaller δ results in a more concentrated and peaked distribution.
5) u, location parameter: It affects the central position.
6) K_λ, the modified Bessel function of the third kind.

B. *Influence of Model Parameters on the Hysteresis Loop*

It is reasonable to consider a symmetrical nature for the PDF of the classical Preisach model. Therefore, the location parameter u is set as 0, and the PDF is symmetrical about the vertical axis. To investigate the influence of individual model parameters on the shape of the hysteresis loop, the initial values of the PDF parameters are set as follows: $\lambda = 3.1$, $\zeta = 0.06$, $\beta = 0$, $\delta = 2.3$, and $u = 0$. The numerical integration approach described in Section III is employed to determine the irreversible component of the hysteresis loop. By analyzing the sensitivity of the hysteresis characteristics to each parameter, the optimal parameter set of the Preisach model can be determined. The effects of different parameters on the hysteresis loop shape are illustrated in Fig. 7.

To facilitate comparative analysis of how model parameters influence the shape of the hysteresis loop, three characteristic quantities are selected: remanence B_r, coercivity H_c, and maximum magnetic flux density $B_{\max}$. The influence of each model parameter on these quantities is summarized in Table III, where "↑" denotes an increase, "↓" denotes a decrease, and "—" indicates negligible or no noticeable change.

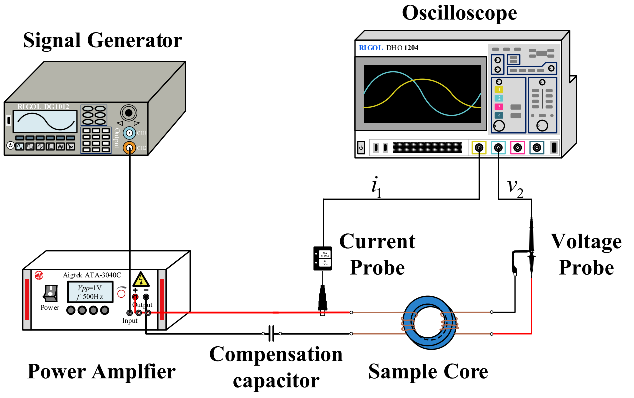

Fig. 8. Schematic of the hysteresis loop measurement platform.

As shown in Fig. 7(a) and (d), the parameters λ and δ significantly affect both B_r and $B_{\max}$, with the impact exhibiting a negative correlation. Fig. 7(b) indicates that ζ has a notable effect on all three characteristic quantities. Meanwhile, Fig. 7(c) reveals that β primarily influences B_{r} and H_{c}, and both parameters are positively correlated with these features.

Applying GH with the proposed parameter identification method, different hysteresis shapes are realized by defining different parameters. Thus, with two additional degrees of freedom, a more accurate hysteresis fitting is achieved, and only one PDF is needed for different materials.

V. SIMULATION AND EXPERIMENTAL VALIDATION

A. *Experimental Setup and Evaluation Criteria*

To validate the proposed implementation method and PDF of the Preisach model, a test platform based on the two-winding method is established to measure the hysteresis loops of the core materials, as shown in Fig. 8.

The measurement process is carried out according to the guidelines in [42]. Two types of magnetic cores, including toroidal ferrite and rectangular silicon steel, are selected. The excitation voltage is obtained using a power amplifier (Aigtek ATA-3040C), taking the signal from a function generator (RIGOL DG1012). A current probe (CYBERTEK HCP8030) is employed for primary side I, which is further converted into field strength H

$$H = \frac{I \cdot N_1}{l} \tag{25}$$

where l is the effective magnetic path length of the core sample, and N_1 is the turn number of the primary winding. The second winding is open and the voltage is measured using a voltage probe (PVP2350). The flux density B is obtained by integrating the measured voltage, as follows:

$$B = \frac{1}{S_a \cdot N_2} \int U dt \tag{26}$$

where S_a is the effective cross-sectional area of the core sample, and N_2 turns the number of the secondary winding.

As this article focuses on frequency-independent hysteresis modeling, the eddy current and residual effects shall be ignored.

Bertotti, through an in-depth analysis of the magnetic domain structure and domain wall motion in ferromagnetic materials combined with statistical theory, proposed a complete loss separation model. The total core loss consists of three main components: hysteresis loss, eddy current loss, and excess loss [13], as expressed by

$$\begin{aligned} P &= P^{(\mathrm{hyst})} + P^{(\mathrm{eddy})} + P^{(\mathrm{exc})} \\ &= k_h f B_{\max}^2 + k_e f^2 B_{\max}^2 + +k_{\mathrm{ex}} f^{1.5} B_{\max}^{1.5} \end{aligned} \tag{27}$$

where P^{hyst} denotes hysteresis loss, P^{eddy} represents eddy current loss, and P^{exc} corresponds to excess loss. The coefficients k_h, k_e, and k_{ex} are the hysteresis, eddy current, and excess loss coefficients, respectively, where k_{ex} is strongly influenced by material thickness, cross-sectional area, and conductivity. f is the excitation frequency.

According to the loss separation model, hysteresis loss P^{hyst} is linearly proportional to the excitation frequency f, while eddy current loss P^{eddy} grows quadratically with f^2, and excess loss P^{exc} typically exhibits a mixed dependence on both f and f^2. Since the focus of this study is frequency-independent hysteresis modeling, both P^{eddy} and P^{exc} should be minimized under the designed experimental conditions. Specifically, when $B_{\max}$ is kept constant, if the measured total core loss exhibits a linear relationship with frequency within the low tested range, this provides strong evidence that P^{eddy} and P^{exc} are negligible, and the total loss is dominated by P^{hyst}.

To determine the appropriate excitation frequency, the peak magnetic flux density for the three materials is fixed at 0.1T, while the excitation voltage is scaled proportionally with frequency. For loss measurements under high-frequency conditions, the two-winding method is highly sensitive to phase deviation. A small phase difference can lead to significant loss errors. Therefore, a coaxial shunt (T&M Research W–0-1STUD) with high bandwidth and purely resistive characteristics is used for high-frequency current measurement [19].

Fig. 9(a) illustrates the relationship between core loss per unit volume P_V (kW/m^3) and frequency for the ferrite material 3F3. Within the 1–100 kHz frequency range, the core loss exhibits an approximately linear dependence on frequency, with the orange curve representing the linear fitting result (correlation coefficient result R^2 of 99.9%). As the frequency increases, the measured losses gradually deviate from the linear trend, which can be attributed to the combined effects of eddy current losses and residual losses, leading to a faster-than-linear growth of the total loss. Fig. 10(a) shows the frequency-dependent loss characteristics of the ferrite core N87, which displays a similar trend to that of 3F3. Therefore, for both ferrite materials, the core loss demonstrates an approximately linear dependence on frequency in the range of 1–100 kHz (correlation coefficient result R^2 of 99.9%).

Fig. 11(a) presents the relationship between P_V and frequency for the silicon steel M330/35. The primary voltage is supplied for silicon steel by the programmable ac power supply IT7627. Within the 1–150 Hz frequency range, the transformer loss exhibits a linear dependence on frequency (correlation coefficient result R^2 of 99.9%). As the frequency increases, the proportion of eddy current losses becomes significantly higher compared to ferrite materials. Moreover, as reported in [43], magnetic hysteresis characteristics should ideally be measured at ultralow frequencies (e.g., 0.01 Hz) where eddy-current effects can be completely neglected. However, such measurements are difficult in practice due to the low signal-to-noise ratio. By contrast, performing hysteresis loop measurements at 20 Hz allows us to effectively ignore eddy-current effects while still ensuring adequate signal levels for accurate measurements.

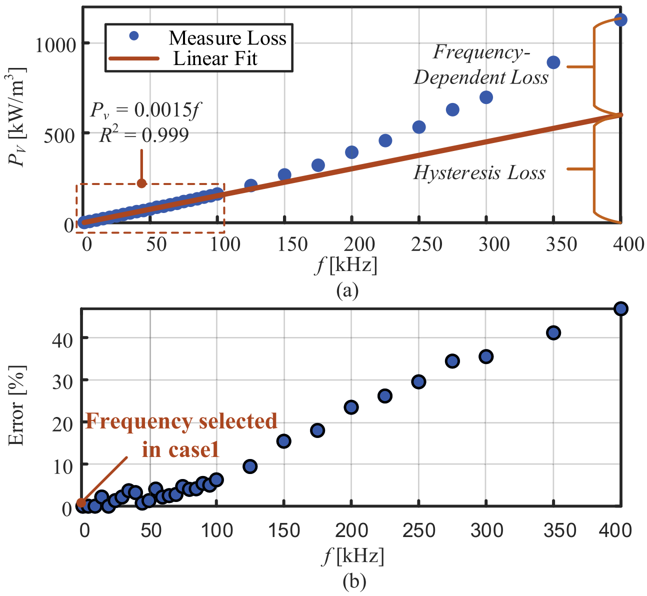

Fig. 9. (a) Relationship between P_V and frequency for 3F3. (b) Error in linear fit and measure loss at different frequencies for 3F3.

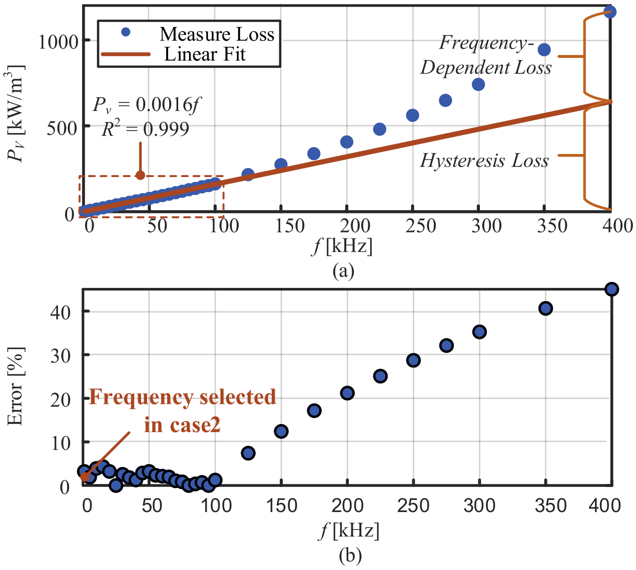

Fig. 10. (a) Relationship between P_V and frequency for N87. (b) Error in linear fit and measure loss at different frequencies for N87.

Hence, the excitation voltage is set as 500 Hz for ferrite and 20 Hz for silicon steel. The influence of parasitic parameters in the test circuit is minimal below 500 Hz, so the resulting phase errors can be neglected [22], [44]. Furthermore, the size

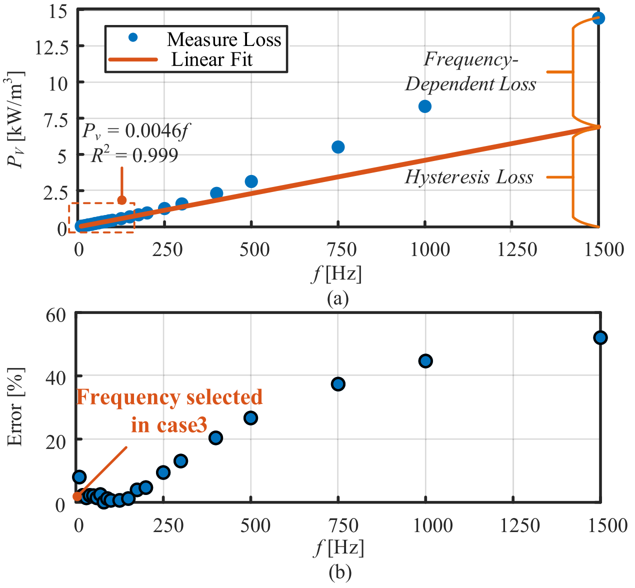

(a)

(b)

Fig. 11. (a) Relationship between P_V and frequency for M330/35. (b) Error in linear fit and measure loss at different frequencies for M330/35. At 10 Hz, the measured loss is 0.05 W, while the predicted value is 0.046 W, resulting in an absolute error of 0.004 W. Although the absolute deviation is small, the relative error appears relatively large due to the small magnitude of the actual loss.

of measured ferrite cores is relatively small, resulting in limited turns on both primary and secondary windings. Simultaneously, the working magnetic density value is relatively low. To avoid measurement and reading errors caused by low applied voltage, excessively low excitation frequencies are not suitable. Therefore, the chosen frequency and test setup ensure that the measurement conditions are consistent with the frequency-independent hysteresis modeling.

Two criteria are defined to evaluate the proposed methods from two perspectives.

1) *Physical aspect:* The per-cycle energy loss is quantified by the area enclosed by the hysteresis loop on B–H plane.
2) *Fitting aspect:* The fitting accuracy is quantified by the sum of squared errors ($SSE = MSE \times N$).

B. Case 1: Ferrite Ring Core From Ferroxcube 3F3

The first validation case uses Ferroxcube 3F3 ferrite material TX36/23/15. The primary and secondary windings are both six turns. The parameter identification process requires only one set of hysteresis loop data. Therefore, the limiting hysteresis loop with a field strength amplitude $H_{100\%} = 100$ A/m is measured for fitting, while minor loops under 80%, 60%, 40%, and 20% of $H_{100\%}$ are used for validation. The PDF parameters remain the same in the following other validation cases, as shown in Table IV. In Fig. 12, the simulated hysteresis loops of the 3F3 under different field strengths are compared with experimental measurements. The peak points of the simulated loops closely overlap with the measured ones, ensuring high accuracy in the prediction of the equivalent magnetic permeability.

In Fig. 13, the simulation errors of per-cycle energy loss using different PDFs are compared with experimental measurements.

TABLE IV
MODEL PARAMETER VALUES IDENTIFIED FROM THE LIMITING HYSTERESIS LOOP FOR 3F3

PDF	Irreversible component (Preisach model)				Reversible component	
GH	λ	ζ	β	δ	K_1	K_2
	6.6376	0.0992	0.0014	1.5264	0.1056	0.0321
Logistic	A	H_0		σ	K_1	K_2
	0.0308	1.9574		0.0444	0.1056	0.0321
Lorentz	A	H_0		σ	K_1	K_2
	0.0085	0.8059		0.0009	0.1056	0.0321

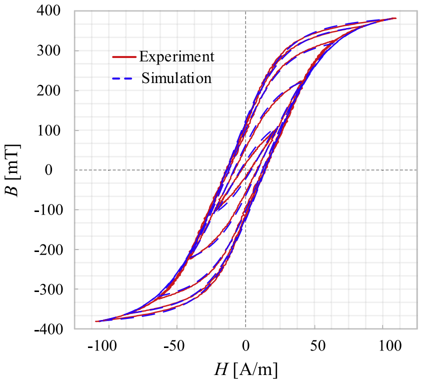

Fig. 12. Comparison between measurement and simulation of 3F3 at different field strength amplitudes using the GH PDF.

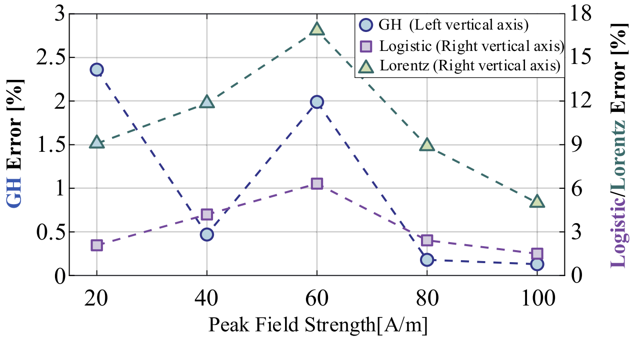

Fig. 13. Percentage error of the simulated per-cycle energy loss of 3F3.

For the GH PDF, the maximum error is 2.36% at $H_{20\%} = 20$ A/m, whereas the maximum errors for the Logistic and Lorentz PDFs are 6.32% and 16.86%, respectively.

Fig. 14 compares the hysteresis loops obtained using GH and Lorentz PDFs. The Lorentz PDF has a higher per-cycle energy loss compared to the GH PDF. The main reason lies in the insufficient accuracy in modeling the loop curvature and higher permeability $\mu_{100\%}^{\uparrow}$ on the ascending branch when using the Lorentz PDF, which results in a larger enclosed area on the B–H plane. The permeability $\mu_{100\%}^{\downarrow}$ on the descending branch is determined by the reversible component.

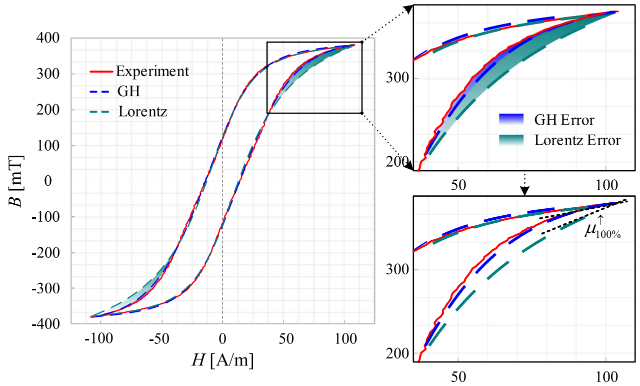

Fig. 14. Comparison of hysteresis loop for 3F3 using GH and Lorentz PDFs.

TABLE V
MODEL PARAMETER VALUES IDENTIFIED FROM THE LIMITING HYSTERESIS LOOP FOR N87

PDF	Irreversible component (Preisach model)				Reversible component	
GH	λ	ζ	β	δ	K_1	K_2
	0.6683	0.0498	0.0001	23.9996	0.0868	0.0149
Logistic	A	H_0	σ		K_1	K_2
	0.0410	0.3008	0.0532		0.0868	0.0149
Lorentz	A	H_0	σ		K_1	K_2
	0.0117	0.7182	0.0017		0.0868	0.0149

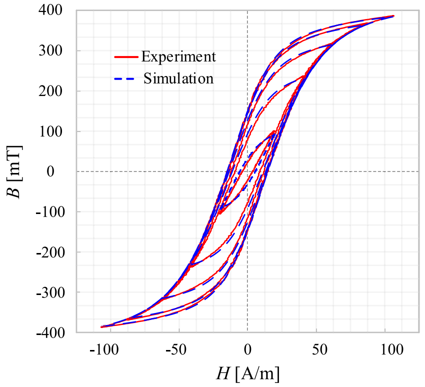

Fig. 15. Comparison between measurement and simulation of N87 at different field strength amplitudes using the GH PDF.

C. Case 2: Ferrite Ring Core From TDK N87

Case 2 uses TDK N87 material, and the shape is R41.8 × 26.2 × 12.5, both primary and secondary are six turns. The parameters are identified based on the limiting hysteresis loop with $H_{100\%} = 100$ A/m as shown in Table V. The parameters of the model remain the same in the other verification cases. In Fig. 15, the model has good agreement with experimental measurements. The maximum per-cycle energy loss error using the GH PDF is 4.52% at $H_{20\,\%}$, with all other loops exhibiting errors below 2.5%. In contrast, the maximum errors for the Logistic and Lorentz PDFs reach 8% and 11.65%, respectively, as shown in Fig. 16. This discrepancy can be attributed to the limited ability to accurately model the permeability on the ascending branch.

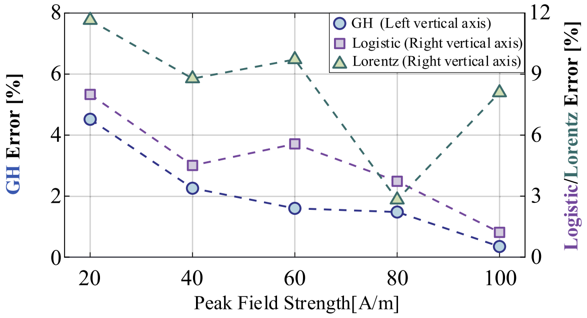

Fig. 16. Percentage error of the simulated per-cycle energy loss of N87.

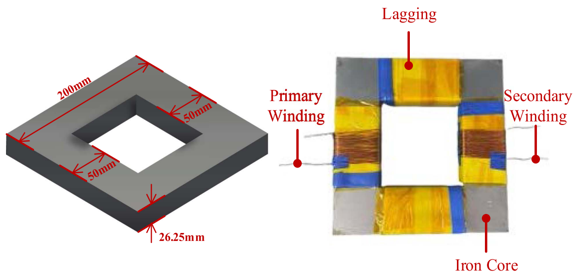

(a) (b)

Fig. 17. (a) Geometric parameter of core sample. (b) Physical configuration of the core sample.

D. Case 3: Silicon Steel Rectangle Core From TKS

In case 3, 75 pieces of silicon steel laminates M330/35 are pressed together, creating the rectangular core sample for verification. The transformer with 30 turns on both the primary and secondary is shown in Fig. 17. The primary voltage is supplied for silicon steel by the programmable ac power supply IT7627. Furthermore, for materials with relatively wide hysteresis loops, the magnetic permeability depends not only on the magnetic field strength but also on the limiting flux density. In such cases, irreversible components require the use of the Product Preisach model [45]. Therefore, in this article, hysteresis loops under different field strengths are individually validated to demonstrate the effectiveness of the proposed parameter identification method and PDF. The parameter values at different peak field strengths are illustrated in Table VI.

In Fig. 18, the experimental comparison under different magnetic field strengths is presented. Compared to the previous two ferrite materials, silicon steel has a significantly wider hysteresis loop. Nevertheless, the proposed implementation approach provides good modeling compared with the measurement results. In Fig. 19, benefiting from the GH PDF, the maximum error in per-cycle energy loss is only 1.8%, whereas the maximum errors for the Logistic and Lorentz PDFs reach 13.27% and 3.18%, respectively.

Fig. 20 compares the hysteresis loops fitted using the GH and the Logistic PDFs. Compared with the GH PDF, the Logistic PDF exhibits higher per-cycle energy loss. The main reason is

TABLE VI
MODEL PARAMETER VALUES IDENTIFIED AT DIFFERENT MAGNETIC FIELD STRENGTHS FOR SILICON STEEL

Peak field strength/[A/m]	PDF	Irreversible component (Preisach model)				Reversible component (arctangent function)	
		λ	ζ	β	δ	K_1	K_2
20	GH	2.1397	0.1002	0.0751	2.4082	0.1649	0.0128
40		0.5976	0.3418	0.2840	24.2863	0.1940	0.0190
60		0.7164	0.6901	0.5639	24.6449	0.2261	0.0241
80		0.7392	0.7951	0.7011	20.7512	0.2503	0.0277
100		0.8929	1.7166	1.6461	11.6644	0.2686	0.0303
		A	H_0	σ		K_1	K_2
20	Logistic	0.0234	44.8927	0.0001		0.1601	0.0097
40		0.0774	46.3255	0.0596		0.1600	0.0099
60		0.0617	35.1524	-0.0755		0.1600	0.0100
80		0.0569	38.4095	-0.0647		0.1600	0.0100
100		0.0518	40.3135	-0.0560		0.1600	0.0100
		A	H_0	σ		K_1	K_2
20	Lorentz	0.4787	39.9269	0.1076		0.1659	0.0131
40		0.0191	27.9950	0.0076		0.1640	0.0125
60		0.0183	34.9833	0.0038		0.1921	0.0094
80		0.0166	39.9883	0.0026		0.1684	0.0138
100		0.0158	45.1323	0.0024		0.1976	0.0196

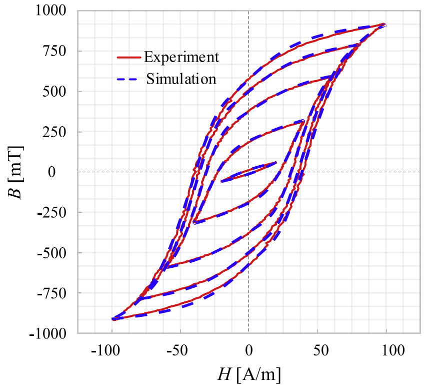

Fig. 18. Comparison between measurement and simulation of silicon steel at different field strength amplitudes using the GH PDF.

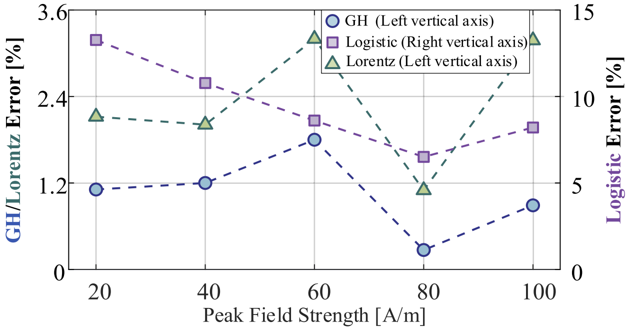

Fig. 19. Percentage error of the simulated per-cycle energy loss of silicon steel.

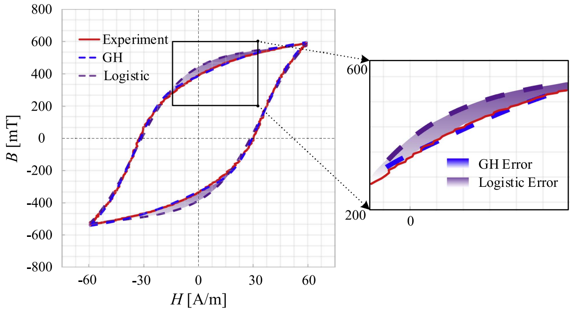

Fig. 20. Comparison of hysteresis loop for silicon steel using GH and logistic PDFs.

that the Logistic PDF fails to accurately capture the curvature characteristics around the remanence region during modeling, resulting in an enlarged enclosed area in the B–H plane. This occurs because the tails of the Logistic PDF decay too rapidly, concentrating the distribution weight near the central region. Consequently, the number of hysteresis operators with extreme threshold values is underestimated, leading to an overestimation of the loop area around remanence and thus larger deviations. In contrast, the GH PDF, with its greater flexibility, can more accurately reproduce the hysteretic characteristics of silicon steel sheets.

Furthermore, per-cycle energy loss alone is not sufficient for evaluating the performance of a hysteresis model. For instance, the model may underestimate losses in the remanence region while overestimating the permeability near the

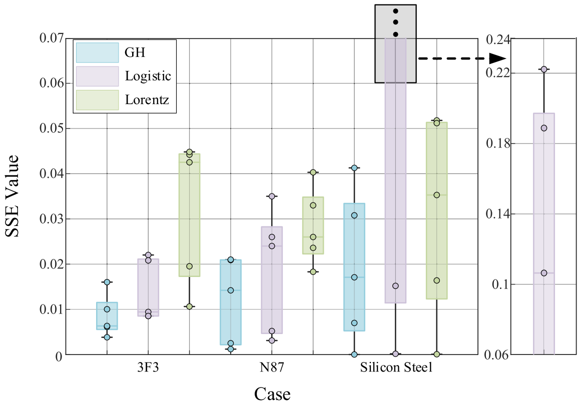

Fig. 21. SSE box chart for GH, Logistic, and Lorentz of different materials. A smaller SSE indicates a higher degree of accuracy.

peak of the ascending branch, leading to amplified local energy dissipation. These opposing errors may cancel each other out in the total energy loss calculation, resulting in a small discrepancy. Hence, such compensation can mask the model's deficiencies in modeling hysteresis behavior. Therefore, it is necessary to evaluate the model from a fitting perspective by comparing the SSE for a more comprehensive assessment.

In Fig. 21, the SSE of two classical PDFs and the proposed GH PDF across three different soft magnetic materials under different magnetic field strengths are compared. Generally, the GH PDF exhibits the lowest SSE values and a narrower interquartile range.

In the modeling of ferrite materials such as 3F3 and N87, both GH and Logistic PDFs outperform the Lorentz PDF, GH and Logistic PDFs achieve lower SSEs of 0.009 and 0.011, respectively, in contrast to the higher SSE of 0.031 observed with the Lorentz PDF.

On the other hand, for silicon steel, the GH and Lorentz PDFs demonstrate comparable performance, whereas the Logistic PDF produces a significantly larger SSE of 0.106, as shown on the right side of Fig. 21. Therefore, the proposed method demonstrates consistent modeling capability for different magnetic materials.

VI. DISCUSSION

In this section, the first two parts compare the proposed method with conventional approaches from the perspectives of simplification and accuracy, providing a macroscopic justification for the proposed approach's superiority. Furthermore, to enhance the model's robustness, the method is extended to enable higher accuracy within specific operating regions. Finally, the potential limitations of the present work are analyzed, and future research directions are outlined.

A. *Simplification of the Proposed Method*

In the continuous Preisach model, different PDFs must be adopted as $p(U, V)$ to accommodate different materials. The conventional discrete Preisach model assumes $p(U, V)$ to be constant within each grid cell and identifies parameters by stacking a large number of measured hysteresis loops, which is excessively complex and computationally inefficient. In contrast, the proposed parameter identification approach requires only a single measurement of the limiting hysteresis loop and introduces the GH PDF as a unified form of $p(U, V)$ for various materials. Moreover, the proposed approach eliminates the complex double integration in continuous Preisach formulations, thereby greatly simplifying the modeling process while maintaining high accuracy.

B. *Accuracy of the Proposed Method*

The traditional continuous Preisach model extracts PDF parameters only from several characteristic points of the limiting and minor hysteresis loops, resulting in low data utilization and fitting distortion at noncharacteristic regions of the curve. In this study, a higher-dimensional and more flexible GH PDF is introduced to enhance the capability of capturing the detailed features of hysteresis loops. By employing the LM algorithm for global optimization using the entire set of data points from a single measured hysteresis loop, the proposed method achieves globally optimal PDF parameters and further improves the overall modeling accuracy.

C. *Approach Extension*

In the proposed method, for ferrite materials, only one limiting hysteresis loop ($H_{100\%} = 100$ A/m) needs to be experimentally measured as input, and the model is parameterized to approximate this loop. Due to the inherent physical characteristics of the Preisach model, the hysteresis loops under different excitation amplitudes can be automatically reproduced without any additional input, maintaining high accuracy.

However, in certain cases where high precision under specific conditions (e.g., $H_{20\%} = 20$ A/m) is required, we further extend this work to discuss its approach expandability and precision tradeoff, aiming to develop the proposed approach into a "white-box model for high-fidelity modeling," capable of enhancing accuracy near specific operating points.

When an application scenario demands high accuracy for the hysteresis behavior at a particular amplitude, the proposed method can be flexibly extended by adding the experimental data corresponding to that amplitude into the objective function (15) during the parameter identification stage, as follows:

$$\begin{aligned}
&\min_{\alpha} S_{\text{ex}}(\alpha) \\
&= \min_{\alpha} \left[\text{MSE}_1(\alpha) + \text{MSE}_2(\alpha) + \ldots + \text{MSE}_n(\alpha)\right] \\
&= \min_{\alpha} \\
&\left\{\begin{array}{l}
\omega_1 \cdot \frac{1}{N_1}\sum_{j_1=1}^{N_1} \left[B_{\exp 1}(j_1) - B_{\text{asc}f1}(H_{j_1}, \alpha)\right]^2 \\
+\omega_2 \cdot \frac{1}{N_2}\sum_{j_2=1}^{N_2} \left[B_{\exp 2}(j_2) - B_{\text{asc}f2}(H_{j_2}, \alpha)\right]^2 \\
+\ldots \\
+\omega_n \cdot \frac{1}{N_n}\sum_{j_n=1}^{N_n} \left[B_{\exp n}(j_n) - B_{\text{asc}fn}(H_{j_n}, \alpha)\right]^2
\end{array}\right\}
\end{aligned} \tag{28}$$

where, $\omega_1, \omega_2, \ldots, \omega_n$ represent the weighting coefficients, and the subscripts 1, 2, ..., n correspond to $H_{100\%}$ and the specific amplitudes of interest, respectively. The measured data at the desired amplitudes are combined with the limiting hysteresis loop data and jointly fitted through global optimization, where the weights can be flexibly assigned according to requirements.

Taking $H_{20\%} = 20$ A/m as a case requiring high-accuracy modeling, for 3F3, with both weights set to 0.5, the SSE at $H_{20\%}$ decreases from 0.0173 to 0.0095, while the SSE values at the other four amplitudes increase accordingly; for N87, with the same weight setting (0.5 for each), the SSE at $H_{20\%}$ decreases from 0.021 to 0.0186, and except for $H_{100\%}$, the SSE values at other amplitudes also decrease slightly, though the improvement is not substantial. In this case, the model no longer relies solely on the information inferred from the limiting hysteresis loop but incorporates local magnetization characteristics from the minor loop, thereby achieving accuracy enhancement in that specific region.

In summary, using only the limiting hysteresis loop as input already yields sufficiently high predictive accuracy. Moreover, the proposed method exhibits strong scalability and adaptability. For scenarios requiring enhanced precision within a specific operating range, multiloop data can be incorporated to realize adaptive optimization. This demonstrates that the proposed implementation is both efficient and robust, while simultaneously ensuring controllable local accuracy.

D. Limitations and Future Work

The proposed implementation of the Preisach model demonstrates significant advantages in terms of modeling simplicity and prediction accuracy. However, these benefits are accompanied by increased computational costs for parameter identification, arising from the enhanced flexibility of the proposed PDF. In contrast to conventional forms such as Lorentz and Logistic PDFs, the GH PDF involves a higher-dimensional structure, which necessitates numerical optimization techniques such as the LM algorithm for parameter identification. This demand becomes important when dealing with large-scale datasets, where computational efficiency issues are more pronounced. In this sense, the additional computational burden for computers can be regarded as the inevitable trade-off for achieving both modeling simplicity for users and prediction accuracy for the result.

With the rapid advancement of artificial intelligence techniques, the development of more efficient optimization algorithms or approximate inference schemes tailored to the GH PDF could be a promising direction to reduce computational costs and broaden the scope of applications.

VII. CONCLUSION

This article proposes an improved implementation method of the Preisach model for the hysteresis model of soft magnetic materials. It uses a novel parameter identification method that avoids restrictive double integration and repeated measurements, while developing the GH PDF for the irreversible magnetization of the Preisach model. Referring to the experimental results concerning different materials, shapes, and hysteresis characteristics, the proposed method, which utilizes only a single measurement, achieves high precision in predicting energy loss and hysteresis behavior across the studied cases. It achieves better performance compared with two conventional modeling methods in terms of accuracy, universality, simplification, and rapidity. In summary, the proposed implementation approach can be used for accurate magnetic hysteresis modeling and is easily implementable in power electronics circuit modeling and simulation.

REFERENCES

[1] M. K. Kazimierczuk, *High-Frequency Magnetic Components*, 2rd ed. Hoboken, NJ, USA: Wiley, 2014, pp. 1–160.

[2] Z. Ouyang and M. A. E. Andersen, "Overview of planar magnetic technology—fundamental properties," *IEEE Trans. Power Electron.*, vol. 29, no. 9, pp. 4888–4900, Sep. 2014.

[3] Z. Shen, H. Wang, Y. Shen, Z. Qin, and F. Blaabjerg, "An improved stray capacitance model for inductors," *IEEE Trans. Power Electron.*, vol. 34, no. 11, pp. 11153–11170, Nov. 2019.

[4] J. Kaiser and T. Dürbaum, "An overview of saturable inductors: Applications to power supplies," *IEEE Trans. Power Electron.*, vol. 36, no. 9, pp. 10766–10775, Sep. 2021.

[5] M. S. Perdigão, J. P. F. Trovão, J. M. Alonso, and E. S. Saraiva, "Large-signal characterization of power inductors in EV bidirectional DC–DC converters focused on core size optimization," *IEEE Trans. Ind. Electron.*, vol. 62, no. 5, pp. 3042–3051, May 2015.

[6] A. Ravera, A. Formentini, M. Lodi, A. Oliveri, M. Passalacqua, and M. Storace, "Modeling the effect of air-gap length and number of turns on ferrite-core inductors working up to magnetic saturation in a buck converter," *IEEE Trans. Circuits Syst. I, Reg. Papers*, vol. 71, no. 12, pp. 5400–5409, Dec. 2024.

[7] T. Rahimi, L. Ding, R. Faraji, M. Kheshti, and J. Pou, "Performance improvement of a three-phase interleaved DC–DC converter without requiring antisaturation control for postfault conditions," *IEEE Trans. Power Electron.*, vol. 36, no. 7, pp. 7378–7383, Jul. 2021.

[8] X. Zhang, X. Su, Y. Wang, H. Wang, and Y. Liu, "Current sensorless online capacitor parameter estimation method in buck converters based on large signal profile considering magnetic saturation," *IEEE Open J. Power Electron.*, vol. 6, pp. 647–659, 2025.

[9] Z. Li, W. Han, Z. Xin, Q. Liu, J. Chen, and P. C. Loh, "A review of magnetic core materials, core loss modeling and measurements in high-power high-frequency transformers," *CPSS Trans. Power Electron. Appl.*, vol. 7, no. 4, pp. 359–373, Dec. 2022.

[10] M. Chen et al., "MagNet challenge for data-driven power magnetics modeling," *IEEE Open J. Power Electron.*, vol. 6, pp. 883–898, 2025.

[11] C. P. Steinmetz, "On the law of hysteresis," *Proc. IEEE*, vol. 9, no. 1, pp. 1–64, Jan. 1892.

[12] J. Muhlethaler, J. Biela, J. W. Kolar, and A. Ecklebe, "Improved core-loss calculation for magnetic components employed in power electronic systems," *IEEE Trans. Power Electron.*, vol. 27, no. 2, pp. 964–973, Feb. 2012.

[13] G. Bertotti, "General properties of power losses in soft ferromagnetic materials," *IEEE Trans. Magn.*, vol. 24, no. 1, pp. 621–630, Jan. 1988.

[14] T. Guillod, P. Papamanolis, and J. W. Kolar, "Artificial neural network (ANN) based fast and accurate inductor modeling and design," *IEEE Open J. Power Electron.*, vol. 1, pp. 284–299, 2020.

[15] H. Li et al., "How MagNet: Machine learning framework for modeling power magnetic material characteristics," *IEEE Trans. Power Electron.*, vol. 38, no. 12, pp. 15829–15853, Dec. 2023.

[16] D. C. Jiles and D. L. Atherton, "Theory of ferromagnetic hysteresis," *J. Magn. Magn. Mater.*, vol. 61, no. 1/2, pp. 48–60, Sep. 1986.

[17] D. L. Atherton and J. R. Beattie, "A mean field Stoner-Wohlfarth hysteresis model," *IEEE Trans. Magn.*, vol. 26, no. 6, pp. 3059–3063, Nov. 1990.

[18] F. Preisach, "Über die magnetische Nachwirkung," *Z. Phys.*, vol. 94, pp. 277–302, 1935.

[19] C. Li, M. Cheng, W. Qin, Z. Wang, X. Ma, and W. Wang, "Core loss model for nonsinusoidal excitations based on vector magnetic circuit theory," *IEEE Trans. Power Electron.*, vol. 40, no. 11, pp. 16926–16936, Nov. 2025.

[20] C. Li, M. Cheng, W. Qin, Z. Wang, X. Ma, and W. Wang, "Analytical loss model for magnetic cores based on vector magnetic circuit theory," *IEEE Open J. Power Electron.*, vol. 5, pp. 1659–1670, 2024.

[21] S. Wang et al., “MagNetX: Foundation neural network models for simulating power magnetics in transient,” in *Proc. IEEE Appl. Power Electron. Conf. Expo.*, 2025, pp. 2438–2445.

[22] M. Luo, D. Dujic, and J. Allmeling, “Modeling frequency-dependent core loss of ferrite materials using permeance–capacitance analogy for system-level circuit simulations,” *IEEE Trans. Power Electron.*, vol. 34, no. 4, pp. 3658–3676, Apr. 2019.

[23] M. Luo, D. Dujic, and J. Allmeling, “Modeling frequency independent hysteresis effects of ferrite core materials using permeance–capacitance analogy for system-level circuit simulations,” *IEEE Trans. Power Electron.*, vol. 33, no. 12, pp. 10055–10070, Dec. 2018.

[24] Princeton University, “MagNet challenge 2,” 2025. [Online]. Available: https://minjiechen.github.io/magnetchallenge-2/

[25] S. Steentjes, M. Petrun, D. Dolinar, and K. Hameyer, “Effect of parameter identification procedure of the static hysteresis model on dynamic hysteresis loop shapes,” *IEEE Trans. Magn.*, vol. 52, no. 5, May 2016, Art. no. 7300804.

[26] F. Liorzou, B. Phelps, and D. L. Atherton, “Macroscopic models of magnetization,” *IEEE Trans. Magn.*, vol. 36, no. 2, pp. 418–428, Mar. 2000.

[27] M. Luo, D. Dujic, and J. Allmeling, “Permeance based modeling of magnetic hysteresis with inclusion of eddy current effect,” in *Proc. IEEE Appl. Power Electron. Conf. Expo.*, 2018, pp. 1764–1771.

[28] N. Djekanovic, M. Luo, and D. Dujić, “Thermally-compensated magnetic core loss model for time-domain simulations of electrical circuits,” *IEEE Trans. Power Electron.*, vol. 36, no. 7, pp. 8193–8205, Jul. 2021.

[29] R. Zeinali, D. C. J. Krop, E. Lomonova, and H. B. Ertan, “Improved Preisach model for modelling magnetic hysteresis effect in non-oriented steels,” in *Proc. 13th Int. Conf. Elect. Mach.*, 2018, pp. 1031–1036.

[30] E. Dlala, “Efficient algorithms for the inclusion of the Preisach hysteresis model in nonlinear finite-element methods,” *IEEE Trans. Magn.*, vol. 47, no. 2, pp. 395–408, Feb. 2011.

[31] G. Consolo, G. Finocchio, M. Carpentieri, and B. Azzerboni, “A genetic approach to solve numerical problems in the Preisach model identification,” *IEEE Trans. Magn.*, vol. 42, no. 5, pp. 1526–1537, May 2006.

[32] R. Liu, C. Gu, J. Sun, F. Shu, and B. Tang, “Analytical inverse Preisach model and its comparison with inverse jiles–atherton model in terms of accuracy and computational speed,” *IEEE Trans. Magn.*, vol. 59, no. 11, Nov. 2023, Art. no. 7300605.

[33] E. Cardelli, L. Fiorucci, and E. Della Torre, “Identification of the Preisach probability functions for soft magnetic materials,” *IEEE Trans. Magn.*, vol. 37, no. 5, pp. 3366–3369, Sep. 2001.

[34] E. Cardelli, G. Finocchio, and E. Pinzaglia, “Increasing the accuracy of the numerical identification of the modified scalar Preisach model,” *IEEE Trans. Magn.*, vol. 40, no. 2, pp. 892–895, Mar. 2004.

[35] B. Azzerboni, E. Cardelli, G. Finocchio, and F. La Foresta, “Remarks about Preisach function approximation using Lorentzian function and its identification for nonoriented steels,” *IEEE Trans. Magn.*, vol. 39, no. 5, pp. 3028–3030, Sep. 2003.

[36] Z. Szabó and J. Füzi, “Implementation and identification of Preisach type hysteresis models with Everett Function in closed form,” *J. Magn. Magn. Mater.*, vol. 406, pp. 251–258, May 2016.

[37] J. Zhang, D. Torres, N. Sepulveda, and X. Tan, “A compressive sensing-based approach for Preisach hysteresis model identification,” *Smart Mater. Struct.*, vol. 25, no. 7, May 2016, Art. no. 075008.

[38] Z. Li, J. Shan, and U. Gabbert, “Inverse compensator for a simplified discrete Preisach model using model-order reduction approach,” *IEEE Trans. Ind. Electron.*, vol. 66, no. 8, pp. 6170–6178, Aug. 2019.

[39] E. Della Torre, J. Oti, and G. Kadar, “Preisach modeling and reversible magnetization,” *IEEE Trans. Magn.*, vol. 26, no. 6, pp. 3052–3058, Nov. 1990.

[40] W. Jouha, A. E. Oualkadi, P. Dherbécourt, E. Joubert, and M. Masmoudi, “Silicon carbide power MOSFET model: An accurate parameter extraction method based on the levenberg–marquardt algorithm,” *IEEE Trans. Power Electron.*, vol. 33, no. 11, pp. 9130–9133, Nov. 2018.

[41] C. Zhang, Y. Li, G. Song, and X. Dong, “Fast and sensitive nonunit protection method for HVDC grids using levenberg–marquardt algorithm,” *IEEE Trans. Ind. Electron.*, vol. 69, no. 9, pp. 9064–9074, Sep. 2022.

[42] E. Stenglein, D. Kuebrich, M. Albach, and T. Duerbaum, “Guideline for hysteresis curve measurements with arbitrary excitation: Pitfalls to avoid and practices to follow,” in *Proc. IEEE Int. Exhib. Conf. Power Electron., Intell. Motion, Renewable Energy Energy Manage.*, 2018, pp. 1–8.

[43] Y. Gao, T. Shibauchi, Y. Gotoh, W. Guan, and K. Muramatsu, “Dynamic hysteresis calculation of silicon steel considering DC hysteresis and anomalous eddy current loss,” *IEEE Trans. Magn.*, vol. 59, no. 5, May 2023, Art. no. 7300105.

[44] M. Mu, Q. Li, D. J. Gilham, F. C. Lee, and K. D. T. Ngo, “New core loss measurement method for high-frequency magnetic materials,” *IEEE Trans. Power Electron.*, vol. 29, no. 8, pp. 4374–4381, Aug. 2014.

[45] M. Luo, “Dynamic modeling of magnetic components for circuit simulation of power electronic systems,” Ph.D. thesis, EPFL, Lausanne, Switzerland, 2018.

Zhan Shen (Senior Member, IEEE) received the B.E. degree from the Nanjing University of Aeronautics and Astronautics, Nanjing, China, in 2013 the M.E. degree from Southeast University, Nanjing, China, in 2016, and the Ph.D. degree from Aalborg University, Aalborg, Denmark, in 2020.

He is currently an Associate Professor with Southeast University. He was a Visiting Scholar with the RWTH Aachen University, Aachen, Germany, and the Massachusetts Institute of Technology, Cambridge, MA, USA. He was with the ABB Corporate Research Center, Beijing, China, in 2016. His research interests include power electronic system integration, magnetic components, and artificial intelligence.

Dr. Shen was the recipient of multiple Best Paper and Best Presenter Awards of the IEEE Power Electronics Society sponsored conferences, and the Outstanding Reviewer Award of the IEEE Transactions on Power Electronics. He is the Guest Associate Editor for IEEE Transactions on Power Electronics, and *CPSS Transactions on Power Electronics and Applications*.

Lexing Zhang was born in Jiangsu, China, in 2003. He received the B.S. degree in electrical engineering and automation from the Nanjing University of Aeronautics and Astronautics, Nanjing, China, in 2024. He is currently working toward the M.E. degree in electrical engineering with the School of Electrical Engineering, Southeast University, Nanjing.

His research focuses on modeling of magnetic components.

Shunshun Ma received the B.S. degree in electrical engineering from Jiangnan University, Wuxi, China, in 2022. He is currently working toward the Ph.D. degree in electrical engineering with Southeast University, Nanjing, under the integrated master’s and doctoral program.

His research focuses on the application of artificial intelligence techniques in battery management systems.

Kaiyuan Liu was born in Jiangsu, China, in 2001. He received the B.S. degree in electrical engineering and automation from the Suzhou University of Science and Technology, Suzhou, China, in 2023. He is currently working toward the Ph.D. degree in electrical engineering with the Southeast University, Nanjing, China.

His research interests include high-frequency magnetic components and power electronic system integration.

Xiao Yu was born in Sichuan Province, China, in 1993. He received the B.S. and Ph.D. degrees from the School of Electrical Engineering, Chongqing University, China, in 2015 and 2020, receptively.

From 2018 to 2019, he was a Visiting Scholar of University of Warwick, Coventry, U.K., in 2018. Since 2020, he has been an Associate Research Fellow with the Electronic Institute, CAEP. His research interests include the reliability of power electronic equipment, the multi-physics modeling and computation of power electronic equipment.

Jian Ai received the Ph.D. degree in electrical engineering from Southeast University, Nanjing, China, in 2021.

In 2022, he has been with Jiangnan University, Wuxi, China, where he is currently an Associate Professor with the School of Internet of Things Engineering. Since 2022, he was a Postdoctoral Fellow with the Department of Electrical Engineering, Nanjing University of Aeronautics and Astronautics, Nanjing, China. His current research interests include resonant converters and dc–dc converters.

Wei Qin (Member, IEEE) received the B.Sc. degree in electrical engineering from Henan Polytechnic University, Jiaozuo, China, in 2016, the M.Sc. degree in power electronics and electrical drives from the Nanjing University of Science and Technology, Nanjing, China, in 2019, and the Ph.D. degree in electrical engineering from Southeast University, Nanjing, in 2024.

Since 2024, he has been a Postdoctoral Fellow with the School of Electrical Engineering, Southeast University. His research interests include magnetic circuit theory and magnetic field modulation theory of electrical machines.

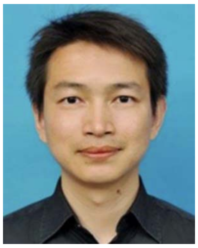

Fujin Deng (Senior Member, IEEE) received the B.Eng. degree in electrical engineering from the China University of Mining and Technology, Jiangsu, China, in 2005, the M.Sc. degree in electrical engineering from Shanghai Jiao Tong University, Shanghai, China, in 2008, and the Ph.D. degree in energy technology from the Department of Energy Technology, Aalborg University, Aalborg, Denmark, in 2012.

From 2013 to 2015 and from 2015 to 2017, he was a Postdoctoral Researcher and an Assistant Professor, respectively, with the Department of Energy Technology, Aalborg University. In 2017, he joined the School of Electrical Engineering, Southeast University, Nanjing, China, as a Professor. His research interests include wind power generation, multilevel converters, high-voltage direct-current technology, dc grid, and offshore wind farm-power systems dynamics.

Long Jin received the master's degree in automation and the Ph.D. degree in vibration, concussion, and noises from the Nanjing University of Aeronautics and Astronautics, Nanjing, China, in 1993 and 1997, respectively.

He is currently a Professor with the School of Electrical Engineering, Southeast University, Nanjing, China. His current research interests include the design and control of high-power electronics, ultrasonic motors, and robotics.

Wu Chen (Senior Member, IEEE) was born in Jiangsu, China, in 1981. He received the B.S., M.S., and Ph.D. degrees in electrical engineering from the Nanjing University of Aeronautics and Astronautics (NUAA), Nanjing, China, in 2003, 2006, and 2009, respectively.

From 2009 to 2010, he was a Senior Research Assistant with the Department of Electronic Engineering, City University of Hong Kong, Hong Kong. In 2010 and 2011, he was a Postdoctoral Researcher with Future Electric Energy Delivery and Management Systems Center, North Carolina State University, Raleigh, NC, USA. Since September 2011, he has been an Associate Research Fellow with the School of Electrical Engineering, Southeast University, Nanjing, China, where he has been a Professor since 2016. His research interests include soft-switching converters, power delivery, and power electronic system integration.

Dr. Chen is an Associate Editor for IEEE TRANSACTIONS ON INDUSTRIAL ELECTRONICS, *Journal of Power Electronics, and CPSS Transactions on Power Electronics and Applications*.